Strong downdrafts preceding rapid tropopause ascent and their potential to identify cross-tropopause stratospheric intrusions

Feilong Chen[1], Gang Chen[1*], Chunhua Shi[2], Yufang Tian[3], Shaodong Zhang[1],

Kaiming Huang[1]

[1]School of Electronic Information, Wuhan University, Wuhan 430072, China.

[2]Key Laboratory of Meteorological Disaster, Ministry of Education, Nanjing

University of Information Science &Technology, Nanjing 210044, China.

[3]Key Laboratory of Middle Atmosphere and Global Environment Observation,

Institute of Atmospheric Physics, Chinese Academy of Sciences, Beijing 100029,

China

*Corresponding author: Gang Chen (g.chen@whu.edu.cn)

Abstract:

The capability of measuring 3-dimensional wind and tropopause structure with relatively high time and vertical resolution makes VHF radar a potentially significant tool for studying various processes of the atmosphere. In the light of present understanding, using VHF radars to identify possible stratospheric intrusions still remain unclear. Here the potential detection of stratospheric intrusion events is discussed using the Beijing MST radar located at Xianghe (39.75°N, 116.96°E). During the passage of a cut-off low in late November 2014, a deep V-shaped tropopause structure, and strong downdrafts (>0.8 m/s) immediately preceding the rapid tropopause ascent (>0.2 km/h) were observed. Within the height region of the downdrafts, the

23 stability of the radar tropopause seems to be weakened. Analysis results from global

24 reanalysis and the satellite data, as well as the trajectory model have shown the clear

25 evidence of the downward stratospheric intrusions (dry ozone-rich and depleted

26 methane air) associated with the strong downdrafts. Twenty typical cases of such strong

27 downdrafts, occurring during various synoptic processes in different seasons, have been

28 presented and 15 of them are exactly associated with some form of stratospheric

29 intrusions. Four years (2012-2015) of such downdrafts are further discussed. The

30 observations reveal that the strong downdrafts preceding the rapid tropopause ascent

31 can be a valuable diagnostic for monitoring intrusion events, which will gain a better

32 understanding of stratospheric intrusions in VHF radar observations.

34 **Keywords:** Stratospheric intrusions; strong downdrafts; rapid tropopause ascent; MST

35 radar; VHF radar; cut-off low

1. Introduction

The tropopause is a stable transition zone separating the vertically stable stratified stratosphere from the active free troposphere. The stratospheric and tropospheric air are remarkably different in their chemical and dynamical characteristics. The stratosphere is dominantly high in ozone and potential vorticity (PV) content and low in water vapor (WV) and methane (CH_4) concentration, while the troposphere is just on the contrary (Holton et al., 1995). Consequently, the natural stable tropopause layer, characterized by strong gradients of trace constituents and wind speeds, plays an important role in stratosphere-troposphere exchange (STE) processes. In other words, the layer is a significant barrier for the atmospheric transport between stratosphere and troposphere (Mahlman, 1997). From a long-term point of view, the seasonal variation of the tropopause height determines the seasonal variation of the flux of stratospheric air into the free troposphere (Appenzeller et al., 1996). Under the global climate warming (e.g. the continuing rise in CO_2), the tropopause variation is also a significant factor that must be considered with regards to the recovery of the stratospheric ozone (Butchart et al., 2010; Chipperfield et al., 2017). On the other hand, the short-term tropopause variability is sensitive to various meso– and small–scale atmospheric processes, during which the folding/intrusion events commonly occur. This characteristic of the tropopause change are sometimes directly used to detect the tropopause folds (e.g. Rao et al., 2008; Alexander et al., 2012, and references therein), but are less, if any, directly used to identify stratospheric intrusions. More detailed analysis of the variability of high-resolution tropopause height and of course some other parameters (e.g. 3-

59   dimentional wind), and how the stratospheric air is transported across the tropopause

60   into the troposphere will help us to yield better understanding of the downward

61   stratospheric intrusions (e.g. Sprenger et al., 2003; Leclair de Bellevue et al., 2007; Das

62   et al., 2016).

63   Although photochemical production within the troposphere is the main source of

64   tropospheric ozone, the influence of downward stratospheric intrusions on tropospheric

65   ozone content cannot be ignored (Oltmans and Levy II, 1992; Stevenson et al., 2006).

66   Stratospheric intrusions bring dry ozone-rich air down into the free troposphere (e.g.

67   Stohl et al., 2000; Sørensen and Nielsen, 2001) and sometimes even deep to the surface

68   (e.g. Gerasopoulos et al., 2006; Grant et al., 2008; Jiang et al., 2015; Das et al., 2016;).

69   By now, it is well established that these intrusions of stratospheric origin will

70   significantly influence other trace gases (such as hydroxyl (OH)) in the troposphere

71   (Holton et al., 1995). These influences then will further contribute to the change of

72   radiative balance (Ramaswamy et al., 1992) and play an important role in the radiative

73   forcing of global climate change (Holton et al., 1995). It is true that stratospheric

74   intrusion events occur all over the world and in any seasons. However, they are highly

75   episodic in both vertical and isentropic (horizontal) directions (Chen, 1995). Various

76   dynamical and physical processes have been proposed to be responsible for extra-

77   tropical intrusion events. These mainly include tropopause folds, stratospheric

78   streamers and break-up, cut-off lows (COLs), wave breaking, and mesoscale convective

79   activities and thunderstorms (Stohl et al., 2003).

80   The certain dynamical and chemical characteristics of stratospheric air allow the

tracers, such as dry ozone-rich and high PV, to be proper indicators for the intrusions penetrating down into the troposphere. Based on these tracers, various tools are available to detect intrusion events. Balloon-borne ozonesonde sounding is an effective tool to make measurements of ozone with high vertical resolution, but is limited by coverage (He et al., 2011) and temporal resolution. In contrast, the satellite-borne remote sensing instruments, such as Atmospheric Infrared Sounder (AIRS), can provide nearly global coverage of various trace gases but have limitations in vertical and temporal resolution. Another method for studying transport processes is trajectory model, from which the backward trajectories can provide valuable information on the possible sources of the trace gases (e.g. Elbern et al., 1997).

By far, large-scale STE has been widely studied and is fairly well understood, but the details of small scale intrusions still need more researches (e.g. Holton et al., 1995). Kumar and Uma (2009) reported that the shortage of direct measurements of vertical winds near the tropopause may be responsible for the lack of fine-scale observations of smaller scale intrusions.

Very-High-Frequency (VHF) radars, compared to the tools mentioned above, are capable of continuously monitoring the atmosphere under any weather conditions and detecting tropopause height from backscattered signal with both high temporal and spatial resolution. During the past two decades, VHF radar measurements were commonly used to assist to study the stratospheric intrusions (e.g. Hocking et al., 2007; Das et al., 2016). However, it still remains uncertain in many aspects when using only the VHF radar to identify intrusion events, especially the criteria for the identification.

103   Complicated and changeable atmospheric processes make it difficult to identify the

104   intrusion events by only radar data. The research by Hocking et al., (2007) have

105   achieved a development in this issue and reported that the rapid ascent in RT altitude

106   (>0.2 km/h) can be a valuable diagnostic for possible stratospheric intrusions. They

107   observed the RT height started to ascent just when the stratospheric air intruded across

108   the tropopause layer directly, although the ascent seems to be a recovery from the drop

109   in tropopause height (many cases, not all, including this study). On the other hand, in

110   fact, tropopause drops are more close related to various atmospheric processes such as

111   cutoff low and low/high trough, rather than the corresponding intrusion process itself.

112   Therefore, tropopause ascent is one of the key objects in this study.

113   The central objective of the present study is to discuss the signature of downward

114   cross-tropopause intrusions using both the measurements of tropopause height and

115   vertical wind by the Beijing MST radar. This study is carried out mainly via a detailed

116   case observation during the passage of a COL and other general cases associated with

117   various atmospheric processes. Our discussion mainly focused on the potential of the

118   MST radar data to identify possible intrusion events, which is the main point of this

119   paper. In section 2 the datasets used in this paper are described, section 3 presents

120   detailed results and discussion, and section 4 gives the conclusions.

121

2. Dataset

2.1. MST radar data and tropopause detection

The Beijing MST radar located at Xianghe, China (39.75° N, 116.96° E, 22 m above sea level) is a VHF radar operated at 50 MHz and installed in 2010 based on the first phase of Chinese Meridian Space Weather Monitoring Project (Chinese Meridian Project for short) (Wang, 2010). The radar antenna array consists of 24×24 three-element Yagi to produce an average power aperture product of 3.2×10^8 Wm^2 and maximum directive gain of 34.8 dB. It operates radiation pattern with 172 kW peak power and 3.2° half-power beam width. More detailed information of the radar system can be found in Chen et al. (2016). Routine low mode data were used for present study with 0.5 h time resolution and 1 μs coded pulse, which provides 150 m vertical resolution. Details of the low mode setup used in this study are given in Table 1.

It has long been known that VHF radar reflectivity is proportional to the mean generalized refractive index gradient M, which is a function of humidity variation and static stability and given by (Ottersten, 1969) as follows

$$M = -77.6 \times 10^{-6}(p/T)(dln\theta/dz)$$

$$\cdot \{1 + 15500q/T[1 - (dlnq/dz)/ (2dln\theta/dz)] \} \qquad (1)$$

where p is the atmospheric pressure (hPa) T is the temperature (K), θ is the potential temperature (K) and q is the specific humidity (gg^{-1}). According to the second and third terms of the equation (1): large humidity variation contributes to the echo from the lower and middle troposphere. From the first term: the radar backscatter power is proportional to the static stability, which in fact is directly proportional to the potential

temperature gradient. The tropopause, near which a strong potential temperature gradient exists, will lead to strong radar echoes in vertical incidence, as well as large radar aspect sensitivity (as shown in Figure 1). Radiosonde data used in this paper were received from the GTS1 type digital radiosonde launched from Beijing Meteorological Observatory (39.93 ºN,116.28 ºE, station number 54511), which is less than 45 km away from the MST radar site. The black line in Fig. 1 denotes the lapse-rate tropopause (LRT) defined using the temperature lapse rate (World Meteorological Organization (WMO), 1986). Applying the characteristic (enhanced radar echoes due to partial specular reflection) mentioned above, the tropopause can be detected and its height determined by VHF radars (Gage and Green, 1979). It has received widespread application around the world, either in middle latitudes (e.g. Hocking et al., 2007), polar regions (e.g. Alexander et al., 2012), and tropical regions (e.g. Yamamoto et al., 2003; Das et al., 2008). Here, the radar-determined tropopause (RT) height is defined as the height (above 500 hPa) where the maximum vertical gradient of echo power located (shown as the orange circle in Figure 1a). This definition of RT is similar to that in the studies of Alexander et al., [2012] and Ravindrababu et al., [2014].

In the present study, the MST radar mainly provides continuous measurements of backscattered echo power, 3-D wind, and RT height with time resolution of 0.5 hour. In addition, the radar aspect sensitivity, expressed as the ratio between vertical (p_v) and oblique (p_o, here used the 15-degree north) beam echo power, is mainly caused by the horizontally stratified anisotropic stable air and thus will be used as potential signature of stratospheric intrusions in the troposphere (e.g. Kim et al., 2001). The backscattered

166 echo power given here is expressed as relative power in decibels (dB). In order to reduce

167 the random noise, the profile of p_v is smoothed by a 3-point running mean in altitude.

168 Note that the data that are heavily contaminated will be eliminated from our datasets.

169 The data of December 2015 and September 2015 are excluded.

170 2.2. AIRS satellite data

171 The AIRS instrument on NASA Aqua/EOS polar orbit satellite is a 2378 channel

172 nadir cross-track scanning infrared spectrometer. It can provide profiles of a number of

173 trace gases, including ozone and CH4 (Susskind et al., 2003). The footprint of these

174 retrieval data is of 45 km by 45 km and their most sensitive region is in an altitude range

175 of 300-600 hPa. Many studies have shown that these AIRS retrieval constituents are

176 useful indicators for detecting stratospheric intrusions. He et al. [2011] suggested that

177 AIRS can observe the enhanced tropospheric ozone that is of stratospheric origin.

178 Xiong et al. [2013] reported that AIRS is capable of observing abnormal depletion in

179 CH4 in the troposphere during intrusions. AIRS offers good latitude-longitude coverage.

180 Here we use version 6 of the AIRS Level-3 ozone and methane retrieval products.

181 2.3. Meteorological reanalysis

182 European Centre for Medium-Range Weather Forecasts (ECMWF) reanalysis

183 ERA-interim data are also used. After November 2000 the data are based on the

184 T511L60 version available with a 6-h temporal resolution and $3^o \times 3^o - 0.125^o \times$

185 0.125^o latitude-longitude grid (Dee et al., 2011). The dataset from 15 isentropic and

186 37 pressure levels interpolated into $0.5^o \times 0.5^o$ grid are applied for present study.

187 2.4. HYSPLIT model

188   Backward (forward) trajectories in given starting locations are capable to

189   reproduce the sources (destinations) of the air parcel that will allow us to examine the

190   intrusions of stratospheric origin in the troposphere (e.g. Elbern et al., 1997). The

191   Hybrid Single Particle Lagrangian Integrated Trajectory model (HYSPLIT) developed

192   by the National Oceanic and Atmospheric Administration (NOAA)'s Air Resource

193   Laboratory (ARL) (Rolph, 2003; Stein et al., 2016) is applied to calculate the backward

194   and forward trajectories. The calculation method of the model is a hybrid between the

195   Lagrangian approach and the Eulerian methodology. In this paper, Global Data

196   Assimilation System (GDAS) datasets are adopted for driving the HYSPLIT.

197

3. Results and discussion

3.1. Meteorological synoptic situation

On the morning of 29 November 2014, a 500-hPa trough developed on the western side of Lake Baikal (Western Siberia). The trough moved southeastward and extended equatorward and its southern tip separated from the westerlies in the afternoon of 30 November 2014 (Fig. 2b), forming a COL near the radar site as shown by the closed geopotential contour. The black stars in Figure 1 and other figures indicate the location of the radar site. On the following days, the COL system moved northeastward gradually (Fig. 2b) and finally stayed over eastern Russia near Sakhalin Island until it reconnected and merged to the westerly flow. 315 K isentropic PV patterns have shown the coarse resolution features of intrusions from the polar reservoir across the tropopause into the midlatitude troposphere. The PV streamer curved and rolled up cyclonically along the western flank of the COL (Fig. 2b).

Fig. 3 shows the time series of hourly surface meteorological parameters over the Beijing station. The data are obtained from the Chinese National Meteorology Information Center and is less than 50 km from the MST radar site. As the dry-cold air invasion accompanied with the COL travelled deeply into the planetary boundary layer, it brought severe weather to the surface, including a rapid decrease in temperature and humidity, and rapid increase in surface wind and sea level pressure. The humidity decreased from ~85 to 12 percent within less than 8 hours. It is well established that the polar-type COLs have strong potential to trigger deep convection (Price and Vaughan, 1993). To examine the potential convection, maps of high quality Climate Data Record

220 (CDR) of daily Outgoing Longwave Radiation (OLR) are displayed in Fig. 4. During

221 the development of the COL, a local region with abnormal low OLR value was clearly

222 observed near the radar site on 29 November (Fig. 4b). The Satellite-observed cloud

223 top temperature also showed the low values corresponding to the low OLR (figure not

224 shown), indicating that convection may be generated near radar side on 29 November.

225 Please note that we did not observe such low value either in OLR (Fig.4c, d) or in cloud

226 top temperature near the radar side on 30 November and 1 December. The time for all

227 the observations in this paper is shown in Universal Time (UTC) which is eight hours

228 behind Beijing standard time (LT=UTC+8).

229 **3.2. MST radar observations**

230 Radar echo power, horizontal wind vector, vertical wind, and radar aspect

231 sensitivity are plotted in Figure 5 as function of height and time during the passage of

232 the COL. Time variation of RT (black line) and LRT (black crosses) heights are also

233 displayed. The RT height first experienced a rapid descent, and then increased rapidly,

234 forming a deep V-shaped structure of ~4 km depth. The vertical velocity of the RT

235 height variation (both the rapid descent and ascent branches) reaches up to 0.28 km/h.

236 The rapid RT variation in altitude is in fact the response of the tropopause fold below

237 the jet stream, which will be well represented in Fig. 8a. Rapid variation in RT height

238 remained a region with low echo power (marked by R on Fig. 5a) and low aspect

239 sensitivity (marked by R' on Fig. 5d) where they should be normally high value within

240 the 'normal' tropopause layer. Unlike the RT height, the radiosonde LRT altitudes are

241 nearly constant during the COL passage. In normal conditions, RT agrees well with the

242   LRT altitude, such as indicated by Fig. 6a. However, large differences, of order of 2.5

243   km (as shown in Fig. 6b at 12 UTC 30 November), are observed between LRT and RT

244   in altitude during the passage of the COL as expected. It is the difference in definition

245   that contribute most to the large differences, especially under the tropopause fold

246   conditions (e.g. Yamamoto et al., 2003 and Fukao et al., 2003). It is worth noting that,

247   in Fig.6b, although there is no clear reversion in the radiosonde temperature profile

248   within the height of RT, the RT height exactly corresponds well to the reversion of

249   zonal and meridional wind and potential temperature gradient. Such differences

250   between RT and LRT heights can commonly be observed, especially during extreme

251   synoptic situations such as cyclone (e.g. Alexander et al., 2012).

252   The most important observation in this detailed case experiment is the strong

253   downdrafts (hereinafter inferred to as main downdrafts) observed immediately

254   preceding the rapid RT ascent (Fig.5c). The radar echo power sharply weakened (dotted

255   rectangle in Fig.5a) and the wind direction changed rapidly (Fig.5b, change from

256   dominant southerly wind to dominant northerly jet) within the height region of the main

257   downdrafts. As mentioned previously, abnormal low value in OLR and cloud top

258   temperature indicates the possible occurrence of convective activity on 29 November,

259   but nothing special appeared on 30 November near radar site. Consequently, we

260   preliminarily consider that the main downdrafts occurred near 07 UT 30 November

261   might not be produced directly by convective activity. Here, the accurate origin of the

262   main downdrafts will not be discussed in detail, and it is also beyond the scope of

263   present study.

264   The research by Hocking et al. (2007) has suggested that the rapid ascent in RT

265   height (>0.2 km h^{-1}) can be a valuable predictor for the occurrence of stratospheric

266   intrusions. Here in this paper, the main downdrafts preceding the rapid RT ascent

267   observed by the Beijing MST radar are thus suspected to be an important feature or

268   response of some form of vertical stratospheric intrusions. Firstly, as the tropopause

269   descends (folded downward), it will displace stratospheric air into the troposphere (e.g.

270   Hoskins et al., 1985). Secondly, the main downdrafts will act as an effective way to

271   weaken the tropopause by means of continuously impinging on the tropopause, through

272   which the stratospheric air is permitted to penetrate down into the free troposphere (e.g.

273   Hirschberg and Fritsch, 1993; Kumar, 2006). In addition, after the main downdrafts,

274   the observed region near the upper troposphere with strong backscatter echoes (marked

275   by Q) and especially with abnormal high aspect sensitivity (marked by Q') may also be

276   a weak signature of the possible intrusions. In normal conditions, they are usually low

277   in value in the upper-troposphere (such as the region marked by P and P'). As we

278   mentioned before, the large value in radar aspect sensitivity is mainly caused by

279   reflection from stable atmospheric layer, such as the tropopause or lower-stratosphere.

280   When stable stratospheric air intrudes into the troposphere and without mixing with the

281   surrounding air mass, the intrusions in the free troposphere will be reflected as

282   abnormal large aspect sensitivity. Further direct evidence of the relevant intrusions in

283   dynamical and chemical aspects will be demonstrated in next section, using satellite

284   AIRS and global reanalysis data.

285   3.3. Associated stratospheric intrusions

286   Due to the sensitivity of the AIRS retrieved ozone and CH_4 is between 300-600

287   hPa. Fig. 7 shows the 500 hPa distribution of AIRS observed ozone and CH_4, along

288   with the AIRS tropopause contour (defined based on the temperature lapse-rate). The

289   ozone distribution maps (left panels of Fig. 7) clearly show a large area with enhanced

290   tropospheric ozone (>80 ppbv) near the radar site during the passage of the COL.

291   Moreover, severe CH_4 depletion (<1840 ppbv) was also observed (right panels in Fig.

292   7). These features of the ozone enhancement, CH_4 depletion, and the corresponding low

293   tropopause altitude clearly support the evidence of vertical downward cross-tropopause

294   stratospheric intrusions on 30 November.

295   The vertical cross-section of ECMWF PV and specific humidity at 1800 UT 30

296   November 2014 and the daily AIRS ozone on 30 November 2014, along a constant

297   latitude 40° N, is shown in Fig. 8. The corresponding vertical structure of the

298   stratospheric intrusions (dry ozone-rich and high PV along with low tropopause) over

299   regions near radar side is clearly seen. The specific humidity tracer displays less distinct

300   structure as compared with the other two tracers (similar as that shown by Vérèmes et

301   al., 2016). The cross-section of PV in Fig. 8a have demonstrated relatively finer-scale

302   structure of the stratospheric PV intrusions (below the jet stream), which penetrated

303   down deeply into ~650 hPa (~3.6 km).

304   3.4. Trajectory model analysis

305   Figure 9 shows 30h backward trajectories ending at the radar site at 18 UT 29

306   November (left panel) and at 18 UT 30 November (right panel). As expected, the air

307   masses parcel transported eastward horizontally before the occurrence of main

308   downdrafts (Fig. 9a). Whereas after the downdrafts, the trajectories clearly show

309   downward intrusions originated from the western side of Lake Baikal. Furthermore, a

310   huge dry intrusion is tracked according to the criterion (based on Lagrangian method)

311   in Raveh-Rubin (2017). Trajectory results further support the evidence of possible

312   stratospheric intrusions that closely related with the main downdrafts.

313   On the other hand, 30-h forward trajectories starting at 00 UT 30 November (left

314   panel) and 00 UT 1 December (right panel) are shown in Fig. 10. It is interesting to note

315   that, from Fig. 10a before the passage of COL, the air parcels at 4 km transport rapidly

316   upward (by more than 4 km within ~23 h) and northeastward to the upper-troposphere

317   of East Siberian. This upward and poleward transportation is associated with a warm

318   conveyor belt (southerly flows dominate) that is located ahead of the COL. It

319   contributes to transporting the tropospheric moist and polluted air (such as aerosol) into

320   the upper-troposphere and even the lower stratosphere (e.g. Stohl et al., 2003; Sandhya

321   et al., 2015). After the downdrafts, forward trajectories in Fig. 10b demonstrate that the

322   dry intrusion air parcels continue to be transported downward and southeastward to the

323   boundary layer or even the surface.

324   3.5. Strong downdrafts preceding rapid tropopause ascent and discussion

325   Figure 11a shows another 20 typical cases of strong downdrafts preceding rapid

326   RT ascent for the period March 2012 and Jan. 2015 (shown placed end-to-end), the

327   LRT height (plotted in crosses) and the vertical velocity of the RT (plotted in orange

328   line) is also plotted. These cases (marked by black rectangular boxes and labeled as S1,

329   S2, S3…, and S20) are identified based on the following criteria: 1) the amplitude of

the RT ascent should exceed 0.6 km (four range gates), 2) vertical velocities of the RT

ascent excess 0.1 km/h, 3) the downdrafts occurred preceding the RT ascent should >0.5

m/s, and the height region of the downdrafts should pass through the RT layer. The

criteria are put forward mainly to avoid the influence of the RT spikes. Figure 11b

shows the backward trajectories for the selected 9 cases. Results show clear evidence

of downward intrusions corresponding to the associated strong downdrafts. Their

sources are mainly from West Siberia (western side of Lake Baikal), except for the case

Tr5. Moreover, according to AIRS daily 500 hPa ozone distribution, most of the cases

in Figure 11a (except for the cases S14, S15, S16, S17, S20) were associated with

significant ozone enhancement, indicating intrusions of stratospheric origin (as shown

in Supplementary figure S1). It is important to note that the RT excursion velocity of

all the cases is not all above 0.2 km/h and some are lower than this value (e.g. cases

S16 and S18). However, some form of stratospheric intrusions was exactly observed in

such cases from both the trajectory and satellite results. Therefore, the threshold of

vertical velocity of the RT ascent is set at 0.1 km/h, rather than 0.2 km/h (Hocking et

al., 2007). Large differences between RT and LRT are also interesting to be noted on

some occasions when the RT changes rapidly (such as the occasion near 14 March

2012).

 According to the meteorological chart, the synoptic situation of those cases

identified in Fig. 11a are introduced. The cases S1, S2, S8, S9, S10, and S11 seem to

have a close relationship with COL development; cases S3, S4, S5, S6, S7, S17, S18,

and S19 seem associated with low or high trough systems (at 500 hPa). The remaining

cases seem not associated with any significant synoptic development. However, in terms of the distribution of isentropic PV (generally at 315K in winter and 330K in summer), we found that the remaining cases S12, S13, S14, S15, S16, and S20 appear to be associated with some form of stratospheric streamers and their break-up within the previous 48h (not shown). Some cases (e.g. S1 and S2) that appear close on the same day were probably caused by the same system. The characteristics of the 20 cases, including background synoptic condition, vertical velocity of the RT ascent, and 500 hPa ozone enhancement, have been summarized in Table 2.

In the light of present understanding, the strong downdrafts preceding the rapid RT ascent can serve as an important diagnostic for intrusion events, during various synoptic processes in any season. This characteristic will be of great use and play an important role in routine identification of stratospheric intrusions. Considering the duration of such downdrafts, a higher time resolution of radar observations will be more helpful. Present study has shown the duration of the majority downdrafts is generally within 1.5-3 hours. We consider, therefore, that the radar resolution should be best within 1h.

Although Hocking et al. (2007) have reported that the rapid tropopause ascent (>0.2 km/h) alone can be a useful diagnostic for potential intrusion events. However, using only the information of RT heights might lead to non-negligible errors, as mentioned above in introduction and according to the observations in Fig. 11. Especially on occasions when the RT ascent is between 0.1-0.2 km/h but the corresponding true intrusions were observed, all such intrusion events will be neglected

374 (maybe ~2 per month, refer to Fig. 12a). Whereas on some occasions when the RT

375 ascent exceeds 0.2 km/h, but without observing true intrusion events (e.g. He et al.,

376 2011), these events will be misdiagnosed (maybe ~13 per month, refer to Fig. 12b). In

377 this sense, using the unique MST radar observations of both the RT height variability

378 and the vertical wind as complementary signature for identifying possible intrusion

379 events is very meaningful.

380   Figure 12 shows four years (2012-2015) of the events with rapid RT ascent (gray

381 bands), and the events with strong downdrafts just preceding the rapid RT ascent (black

382 bands). The identification criteria of such strong downdrafts are similar to that

383 mentioned above and the events are classified according to different value of vertical

384 velocity of the ascent. Among all the events with ascent velocity between 0.1-0.2 km/

385 h, about one-quarter (approximate 2 per month, Fig. 12a) were observed with strong

386 downdrafts preceding them. Whereas, as for the events with the ascent velocity >0.2

387 km/h, the proportion is about a half (approximate 10 per month, Fig. 12b). Here,

388 according to the results above, the occurrence of the strong downdrafts just preceding

389 the rapid RT ascent (black bands in Fig. 12) to a large degree represents the occurrence

390 of possible intrusions. In this way, Fig. 12 indicates that the occurrence of possible

391 intrusions exhibit distinct seasonal variations, with a maximum in winter and spring

392 minimum in summer. This is because the meso- and small-scale atmospheric processes,

393 such as cold air outbreaks, thunderstorms, and convective activities, are more active in

394 winter and spring. They are important sources for downward stratospheric intrusions.

395

4. Conclusions

Detailed case analysis of the cross-tropopause stratospheric intrusions was carried out during a COL. Global reanalysis, satellite data, and HYSPLIT trajectories all showed consistent evidences of dry ozone-rich, high PV, and depleted CH4 air that have penetrated downward into the free troposphere. The key signature of the stratospheric intrusions in the Beijing MST radar observations is the strong downdrafts just preceding rapid RT ascent. The radar echo power decreased rapidly within the region of strong downdrafts, after which abnormal high aspect sensitivity was recorded in troposphere. Such high aspect sensitivity is served as another potential clue for the intrusions of stratospheric origin.

Based on the criteria mentioned in section 3.5, other 20 typical cases of strong downdrafts preceding the rapid RT ascent between March 2012 and January 2015 were presented. These events occurred during different synoptic processes in different seasons. Yet, most of the cases (15 of them) are associated with some form of intrusions observed by combination of AIRS-retrieved ozone and the HYSPLIT trajectory model. Our results show that the radar-derived tropopause height and vertical winds are strong complementary indicators to be used to infer the occurrence of the intrusions of stratospheric origin. This will be of great use and play an important role for the routine identification or prediction of intrusion events. However, the actual origin of the observed downdrafts preceding the rapid RT ascent is not addressed in this paper. Further combination observational experiments need to be conducted, especially combined using ozonesonde soundings, to quantitative analyze the effectiveness of

418   present identification criteria for possible intrusions.

419

420

Acknowledgment

The authors really appreciate Prof Shira Raveh-Rubin for reading and checking the manuscript. This work is funded by National Natural Science Foundation of China (NSFC grants No. 41722404 and 41474132). The authors would like to thanks the technical and scientific staff of Chinese Meridian Space Weather Monitoring Project (CMSWMP) for their support in conducting the experiment. The authors sincerely acknowledge the ECMWF, NASA, and NOAA Air Resources Laboratory (ARL) for providing global reanalysis, satellite trace gases, and HYSPLIT transport model, respectively. The MST radar data for this paper are available at Data Centre for Meridian Space Weather Monitoring Project (http://159.226.22.74/). The radiosonde data is available from http://weather.uwyo.edu/upperair/sounding.html.

References

Appenzeller, C., Holton, J. R., & Rosenlof, K. H.: Seasonal variation of mass transport across the tropopause. Journal of Geophysical Research Atmospheres, 101(D10), 15071–15078, 1996.

Appenzeller, C., Davies, H. C., & Norton, W. A.: Fragmentation of stratospheric intrusions. Journal of Geophysical Research Atmospheres. 101(D1), 1435-1456, 1996.

Alexander, S. P., Murphy, D. J., and Klekociuk, A. R.: High resolution VHF radar measurements of tropopause structure and variability at Davis, Antarctica (69° S, 78° E). Atmospheric Chemistry and Physics, 13(12), 26173-26205, 2012.

Bonasoni, P., Evangelisti, F., Bonafe, U., Ravegnani, F., Calzolari, F., Stohl, A., Tositti L., Tubertini O., & Colombo, T.: Stratospheric ozone intrusion episodes recorded at Mt. Cimone during the VOTALP project: case studies. Atmospheric Environment, 34(9), 1355-1365, 2000.

Butchart, N., Cionni, I., Eyring, V., Shepherd, T. G., Waugh, D. W., & Akiyoshi, H., et al.: Chemistry-climate model simulations of twenty-first century stratospheric climate and circulation changes. Journal of Climate, 23(20), 5349-5374, 2010.

Chipperfield, M. P., Bekki, S., Dhomse, S., Harris, N., Hassler, B., & Hossaini, R., et al.: Detecting recovery of the stratospheric ozone layer. Nature, 549(7671), 211-218, 2017.

Chen, P.,: Isentropic cross-tropopause mass exchange in the extratropics. Journal of Geophysical Research, 16661-16673, 1995.

Chen, G., Cui, X., Chen, F., Zhao, Z., Wang, Y., Yao, Q., ... & Gong, W.: MST Radars of Chinese Meridian Project: System Description and Atmospheric Wind Measurement. IEEE Transactions on Geoscience and Remote Sensing, 54(8), 4513-4523, 2016.

Das, S. S., A. R. Jain, K. K. Kumar, and D. Narayana Rao: Diurnal variability of the tropical tropopause: Significance of VHF radar measurements, Radio Sci., 43, RS6003, doi:10.1029/2008RS003824, 2008.

Das, S. S., Ratnam, M. V., Uma, K. N., Patra, A. K., Subrahmanyam, K. V., Girach, I. A., Suneeth K. V. , Kumar K. K.,. & Ramkumar, G.:Stratospheric intrusion into the troposphere during the tropical cyclone Nilam (2012). Quarterly Journal of the Royal Meteorological Society, 142(698), 2168-2179, 2012.

Das, S.S., M. V. Ratnam, K. N. Uma, K. V. Subrahmanyam, I.A.Girach, A. K. Patra,S. Aneesh, K.V. Suneeth, K. K. Kumar, A.P.Kesarkar, S. Sijikumar and G. RamkuMarch.: Influence of Tropical Cyclones on Tropospheric Ozone: Possible Implications (2016), Atmospheric Chemistry and Physics, 16, 4837-4847, 2016.

Dee, D. P., Uppala, S. M., Simmons, A. J., Berrisford, P., Poli, P., & Kobayashi, S., et al.: The era‑interim reanalysis: configuration and performance of the data assimilation system. Quarterly Journal of the Royal Meteorological Society, 137(656), 553-597, 2011.

Elbern, H., Kowol, J., Sládkovic, R., & Ebel, A.: Deep stratospheric intrusions: a statistical assessment with model guided analyses. Atmospheric Environment, 31(19), 3207-3226, 2006.

477   Fukao, S., H. Hashiguchi, M. Yamamoto, T. Tsuda, T. Nakamura, M. K. Yamamoto,

478   T. Sato, M. Hagio, and Y. Yabugaki.: Equatorial Atmosphere Radar (EAR).:

479   System description and first results, Radio Sci., 38(3), 1053,

480   doi:10.1029/2002RS002767, 2003.

481   Gage, K. S., & Green, J. L.: Tropopause detection by partial specular reflection with

482   Very-High-Frequency radar. Science, 203(4386), 1238-40, 1979.

483   Gerasopoulos, E., Zanis, P., Papastefanou, C., Zerefos, C.S., Ioannidou, A., Wernli, H.:

484   A complex case study of down to the surface intrusions of persistent stratospheric

485   air over the Eastern Mediterranean. Atmospheric Environment, 40(22), 4113-4125,

486   2006.

487   Grant, Deanne, Jose D. Fuentes, Marcia S. DeLonge, Stephen Chan, Everette Joseph,

488   Paul Kucera, Seydi A. Ndiaye, Amadou T. Gaye (2008), Ozone transport by

489   mesoscale convective storms in western Senegal, Atmos. Envir., 42, 7104–7114,

490   doi:10.1016/j.atmosenv.2008.05.044

491   He, H., Tarasick, D. W., Hocking, W. K., Careysmith, T. K., Rochon, Y. J., Zhang, J., ...

492   & Bourqui, M. S.: Transport analysis of ozone enhancement in Southern Ontario

493   during BAQS-Met. Atmospheric Chemistry and Physics, 11(6), 2569-2583, 2011.

494   Hocking, W. K., Careysmith, T., Tarasick, D. W., Argall, P. S., Strong, K., Rochon, Y.

495   J., Zawadzki Irek & Taylor, P. A.: Detection of stratospheric ozone intrusions by

496   windprofiler radars. Nature, 450(7167), 281-284, 2007.

497   Holton, J. R., P. H. Haynes, M. E. McIntyre, A. R. Douglass, R. B. Rood, and L. Pfister:

498   Stratosphere-troposphere exchange, Reviews of Geophysics, 33(4), 403–439,

499   doi:10.1029/95RG02097, 1995.

500   Hoskins B.J., McIntyre M.E., Robertson A.W.: On the use and significance of

501   isentropic potential vorticity maps. Q. J. R. Meteorol. Soc. 111: 877–946. 1985.

502   Hirschberg, P. A., and J. M. Fritsch: A study of the development of extratropical

503   cyclones with an analytic model. Part I: The effects of stratospheric structure,

504   Journal of the Atmospheric Sciences, 50, 311 –327, doi:10.1175/1520-

505   0469(1993)050<0311:ASOTDO>2.0.CO;2, 1993.

506   Jiang, Y. C., T. L. Zhao, J. Liu, X. D. Xu, C. H. Tan, X. H. Cheng, X. Y. Bi6, J. B. Gan,

507   J. F. You, and S. Z. Zhao (2015), Why does surface ozone peak before a typhoon

508   landing in southeast China? Atmos. Chem. Phys., 15, 13331–13338,

509   doi:10.5194/acp-15- 13331-2015

510   Kim, K. E., Jung, E. S., Campistron, B., & Heo, B. H.: A physical examination of

511   tropopause height and stratospheric air intrusion: a case study. Journal of the

512   Meteorological Society of Japan, 79(5), 1093-1103, 2001.

513   Kumar, K. K., & Uma, K. N.: High temporal resolution VHF radar observations of

514   stratospheric air intrusions in to the upper troposphere during the passage of a

515   mesoscale convective system over gadanki (13.5° n, 79.2° e). Atmospheric

516   Chemistry & Physics, 24(8), 14-17, 2009.

517   Kumar, K. K.: VHF radar observations of convectively generated gravity waves: Some

518   new insights. Geophysical Research Letters, 33(1), doi:10.1029/2005GL024109,

519   2006.

520   Leclair de Bellevue J, Baray JL, Baldy S, Ancellet G, Diab R, Ravetta F.: Simulations

of stratospheric to tropospheric transport during the tropical cyclone Marlene event. Atmospheric Environment. **41**: 6510–6526, 2007.

Mahlman, J. D.: Dynamics of transport processes in the upper troposphere. Science, 276(5315), 1079-1083, 1997.

Mihalikova, M., Kirkwood, S., Arnault, J., & Mikhaylova, D.: Observation of a tropopause fold by MARA VHF wind-profiler radar and ozonesonde at Wasa, Antarctica: comparison with ECMWF analysis and a WRF model simulation. Annales Geophysicae, 30(9), 1411-1421, 2012.

Nastrom, G. D., Green, J. L., Gage, K. S., & Peterson, M. R.: Tropopause folding and the variability of the tropopause height as seen by the flatland VHF radar. Journal of Applied Meteorology, 28(12), 1271-1281, 1989.

Oltmans, S. J., and H. Levy II.: Seasonal cycle of surface ozone over the western North Atlantic, Nature, 358, 392–394, 1992.

Ottersten, H.: Mean vertical gradient of potential refractive index in turbulent mixing and radar detection of CAT, Radio Science, 4, 1247–1249, doi:10.1029/RS004i012p01247, 1969.

Price, J. D., & Vaughan, G.: The potential for stratosphere-troposphere exchange in cut-off-low systems. Quarterly Journal of the Royal Meteorological Society, 119(510), 343-365, 1993.

Rao, T. N., and S. Kirkwood: Characteristics of tropopause folds over Arctic latitudes, Journal of Geophysical Research, 110, D18102, doi:10.1029/2004JD005374, 2005.

543 Rao, T. N., Arvelius, J., & Kirkwood, S.: Climatology of tropopause folds over a

544   european arctic station (esrange). Journal of Geophysical Research Atmospheres,

545   113(D7), 762-770, 2008.

546 Ravindrababu, S., Venkat Ratnam, M., Sunilkumar, S. V., Parameswaran, K., and

547   Krishna Murthy, B. V.: Detection of tropopause altitude using Indian MST radar

548   data and comparison with simultaneous radiosonde observations. Journal of

549   Atmospheric and Solar-Terrestrial Physics, 121(6), 679-687, 2014.

550 Ramaswamy V, Schwarzkopf MD, Shine KP.: Radiative forcing of climate from

551   halocarbon-induced global stratospheric ozone loss. Nature **355**: 810–812, doi:

552   10.1038/355810a0, 1992.

553 Rolph, G.D.: Real-time Environmental Applications and Display sYstem (READY)

554   Website. NOAA Air Resources Laboratory, Silver Spring, MD. http://

555   www.arl.noaa.gov/ready/hysplit4.html, 2003.

556 Raveh-Rubin, S.: Dry Intrusions: Lagrangian Climatology and Dynamical Impact on

557   the Planetary Boundary Layer. J. Climate, 30, 6661–6682, 2017.

558 Sandhya, M., Sridharan, S., & Indira Devi, M.: Tropical upper tropospheric humidity

559   variations due to potential vorticity intrusions. Annales Geophysicae, 33(9), 1081-

560   1089, 2015.

561 Skerlak, B., Sprenger, M., Pfahl, S., Tyrlis, E., & Wernli, H.: Tropopause folds in ERA-

562   Interim: Global climatology and relation to extreme weather events. Journal of

563   Geophysical Research, 120(10), 4860-4877, 2015.

564 Stohl, A., Bonasoni, P., Cristofanelli, P., Collins, W., Feichter, J., & Frank, A., et al.:

Stratosphere-troposphere exchange: a review, and what we have learned from staccato. Journal of Geophysical Research Atmospheres, 108(D12), 469-474, 2003.

Stohl, A., et al.: The influence of stratospheric intrusions on alpine ozone concentrations, Atmospheric Environment, 34, 1323– 1354, 2000.

Stohl, A., Wernli, H., James, P., Bourqui, M., Forster, C., & Liniger, M. A., et al.: A new perspective of stratosphere troposphere exchange. Bulletin of the American Meteorological Society, 84(11), 2003.

Stein, A. F., Draxler, R. R., Rolph, G. D., Stunder, B. J. B., Cohen, M. D., & Ngan, F.: Noaa's HYSPLIT atmospheric transport and dispersion modeling system. Bulletin of the American Meteorological Society, 96(12), 150504130527006, 2016.

Stevenson, D. S., Dentener, F. J., Schultz, M. G., Ellingsen, K., Noije, T. P. C. V., & Wild, O., et al.: Multimodel ensemble simulations of present-day and near-future tropospheric ozone. Journal of Geophysical Research Atmospheres, 111(D8), 263-269, 2006.

Sørensen, J. H., and Nielsen, N. W.: Intrusion of stratospheric ozone to the free troposphere through tropopause folds -a case study. Physics and Chemistry of the Earth Part B Hydrology Oceans and Atmosphere, 26(10), 801-806, 2001.

Su, L., Yuan, Z., Fung, J. C., & Lau, A. K.: A comparison of HYSPLIT backward trajectories generated from two GDAS datasets. Science of The Total Environment, 527-537, 2015.

Susskind, J., C. D. Barnet, and J. M. Blaisdell.: Retrieval of atmospheric and surface

parameters from AIRS/AMSU/HSB data in the presence of clouds, IEEE Transactions on Geoscience and Remote Sensing, 41(2), 390–409, doi:10.1109/tgrs.2002.808236, 2003.

Vaughan, G., Gouget, H., O'Connor, F. M., & Wier, D.: Fine-scale layering on the edge of a stratospheric intrusion. Atmospheric Environment, 35(12), 2215–2221, 2001.

Vérèmes, H., J.-P. Cammas, J.-L. Baray, P. Keckhut, C. Barthe, F. Posny, P. Tulet, D. Dionisi, and S. Bielli: Multiple subtropical stratospheric intrusions over Reunion Island: Observational, Lagrangian, and Eulerian numerical modeling approaches, Journal of Geophysical Research Atmospheres, 121, 14,414–14,432, doi:10.1002/2016JD025330, 2016.

Wang, C.: New Chains of Space Weather Monitoring Stations in China. Space Weather-the International Journal of Research and Applications, 8(8), 2010.

World Meteorological Organization (WMO): Atmospheric ozone 1985, WMO Global Ozone Res. and Monit. Proj. Rep. 20, Geneva, Switzerland, 1986.

Xiong, X., C. Barnet, E. Maddy, S. C. Wofsy, L. Chen, A. Karion, and C. Sweeney.: Detection of methane depletion associated with stratospheric intrusion by atmospheric infrared sounder (AIRS), Geophysical Research Letters, 40, 2455–2459, doi:10.1002/grl.50476, 2013.

Yamamoto, M., Oyamatsu, M., Horinouchi, T., Hashiguchi, H., & Fukao, S.: High time resolution determination of the tropical tropopause by the Equatorial Atmosphere Radar. Geophysical Research Letters, 30(21), 2003.

609 **Table**

Radar parameter	Value
Transmitted frequency	50 MHz
Antenna array	24×24 3-element Yagi
Antenna gain	33 dB
Transmitter peak power	172.8 kW
Code	16-bit complementary
No. coherent integrations	128
No. FFT points	256
No. spectral average	10
Pulse repetition period	160 μs
Half power beam width	3.2^o
Pulse length	1 μs
Range resolution	150 m
Temporal resolution	30 min
Off-zenith angle	15°

610 **Table 1.** Operating parameters in low-mode of the Beijing MST radar.

611

Cases	Time (year/month/day)	Background condition	Vertical velocity of RT ascent	500 hPa ozone enhancement
S1	2012/03/06	Cut-off low	>0.2 km/h	Enhanced
S2	2012/03/06	Cut-off low	>0.2 km/h	Enhanced
S3	2012/03/12	Low/high trough	>0.2 km/h	Enhanced
S4	2012/03/13	Low/high trough	>0.2 km/h	Enhanced
S5	2012/04/05	Low/high trough	>0.2 km/h	Enhanced
S6	2012/04/05	Low/high trough	>0.2 km/h	Enhanced
S7	2012/04/06	Low/high trough	>0.2 km/h	Enhanced
S8	2012/06/13	Cut-off low	>0.2 km/h	Enhanced
S9	2012/06/13	Cut-off low	>0.2 km/h	Enhanced
S10	2013/08/02	Cut-off low	>0.2 km/h	Enhanced
S11	2013/08/02	Cut-off low	>0.2 km/h	Enhanced

S12	2013/08/03	PV streamer	>0.2 km/h	Enhanced
S13	2013/08/03	PV streamer	>0.2 km/h	Enhanced
S14	2014/01/02	PV streamer	>0.2 km/h	None
S15	2014/01/02	PV streamer	>0.2 km/h	None
S16	2014/01/03	PV streamer	0.1-0.2 km/h	None
S17	2014/01/04	Low/high trough	>0.2 km/h	None
S18	2014/05/02	Low/high trough	0.1-0.2 km/h	Enhanced
S19	2014/05/02	Low/high trough	>0.2 km/h	Enhanced
S20	2015/01/03	PV streamer	>0.2 km/h	None

612   **Table 2.** Characteristics of the 20 cases shown in Fig. 11a.

613
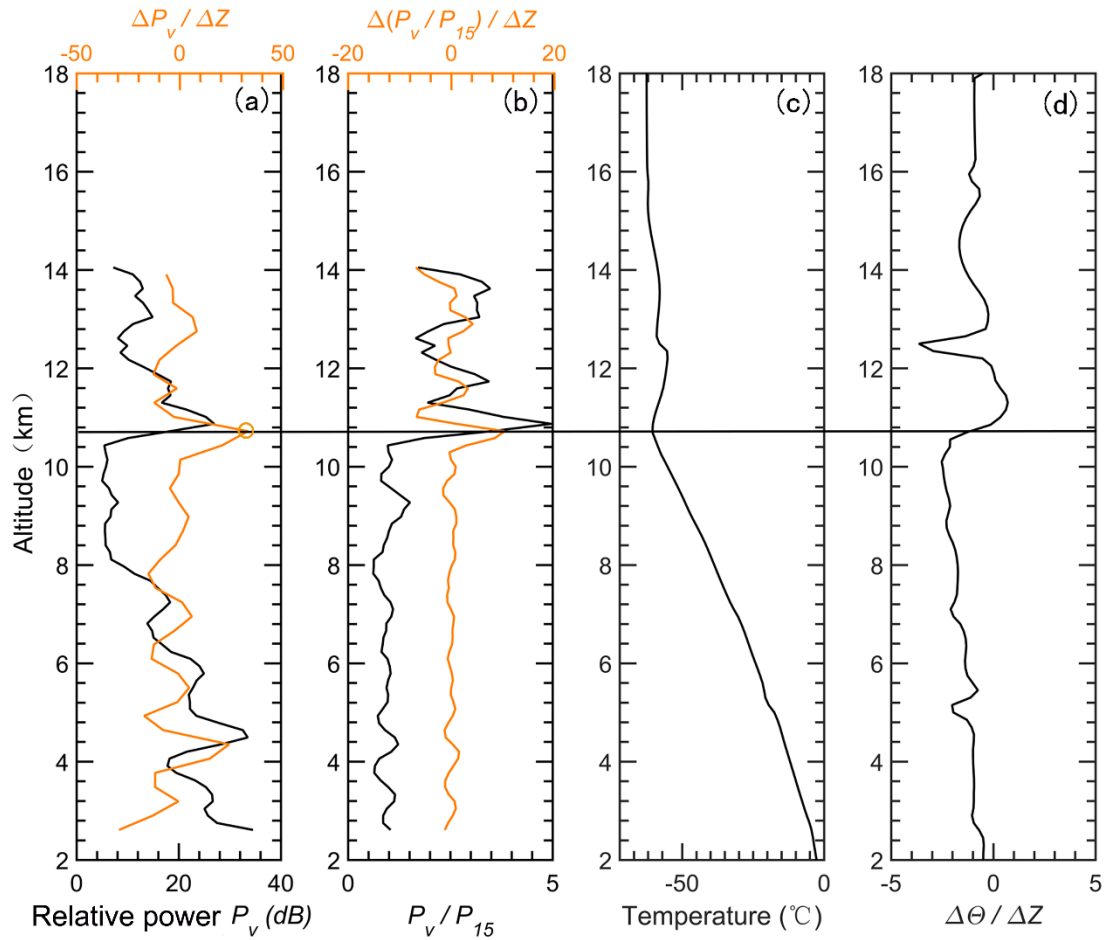
Figures

Figure 1. Example of the vertical height profiles of (a) the relative radar echo power (black line, smoothed by a 3-point running mean) along with its gradient variation (orange line), (b) the aspect sensitivity (black line, expressed as the ratio between the vertical echo power and oblique echo power) along with its gradient variation (orange line), observed on 12 UT 29 November 2014. The vertical profiles of simultaneous radiosonde observed temperature and potential temperature gradient are shown in plots (c) and (d). The black horizontal line denotes the LRT height derived from the radiosonde temperature profile. The orange circle indicates the RT height derived from the profile of the radar backscattered echo power.

625
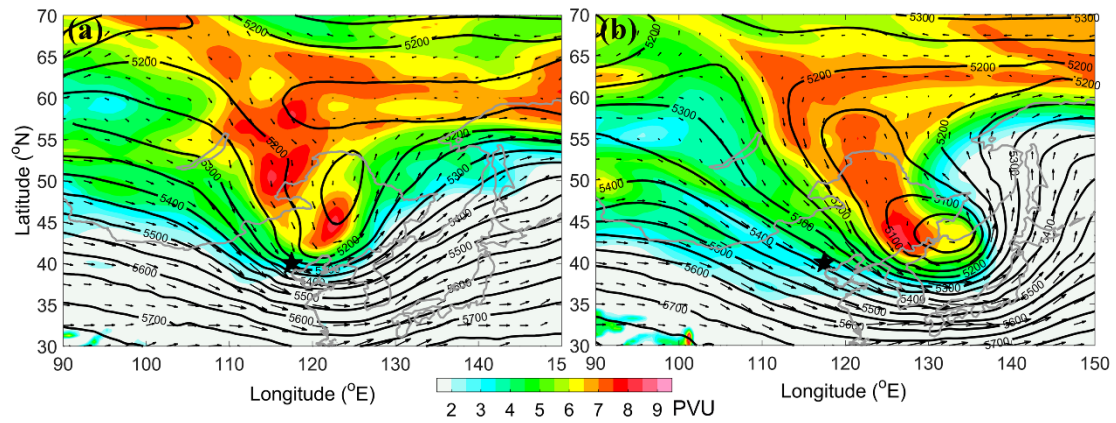
Figure 2. ECMWF derived isentropic PV map on 315 K surface (shaded above 2 pvu,

1 PVU=10^{-6} m^2 K kg^{-1} s^{-1}) and geopotential height (contoured every 50 m in solid line)

along with the wind vector (arrow) at 500 hPa (~5.5 km a.s.l.) on (a) 18 UTC 30

November 2014, (b) 12 UTC 1 December 2014. The black star shows the location of

Xianghe.

631
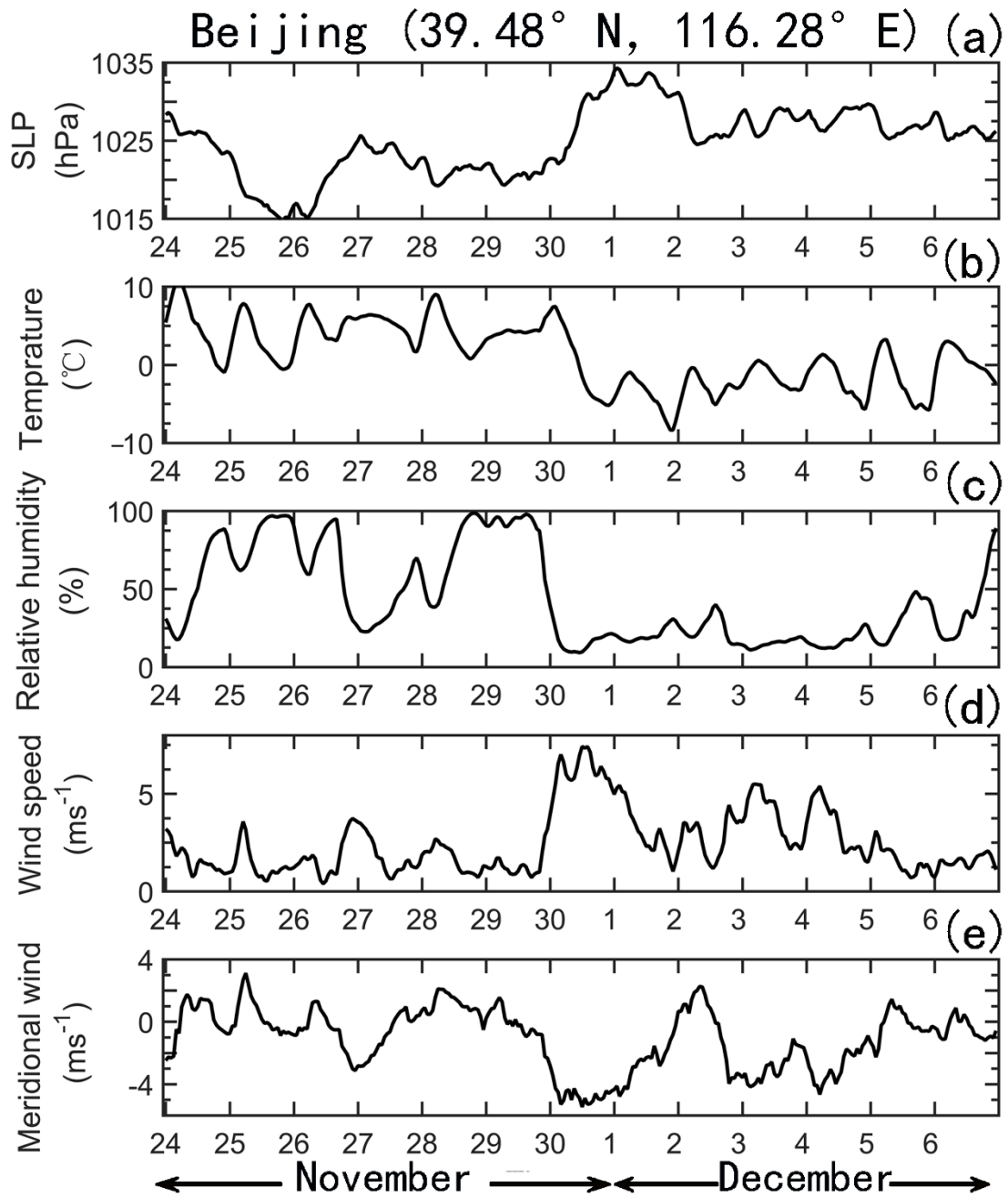
Figure 3. Time series of surface (~1.2 m above the surface) hourly meteorological

measurements of (a) sea level pressure, (b) temperature, (c) relative humidity, (d)

horizontal wind, and (e) meridional wind during the period 24 November-6 December

2014, observed over the Beijing station (39.4° N, 116.2° E, 31.3 m above sea level).

636
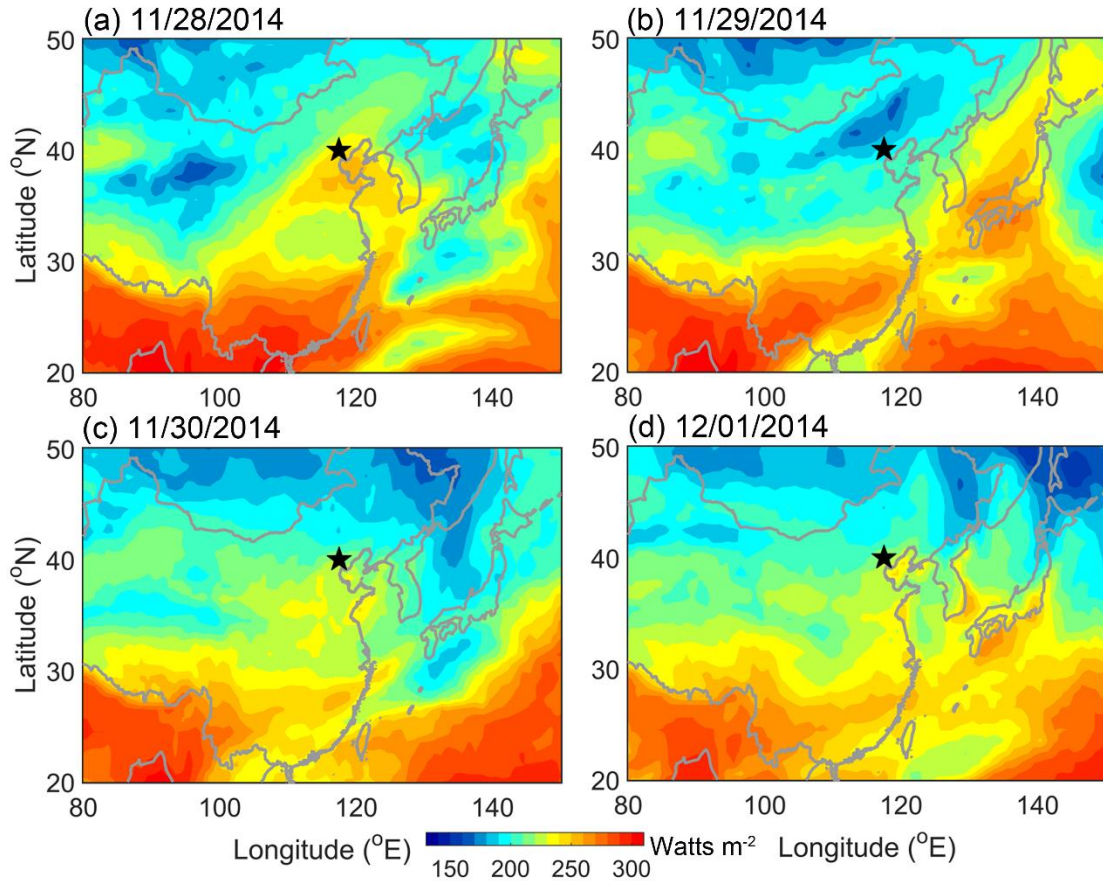
Figure 4. Contour maps of the high quality Climate Data Record (CDR) of the daily Outgoing Longwave Radiation (OLR), derived from the NOAA high-resolution infrared radiation sounder (HIRS) on (a) 28 November, (b) 29 November, (c) 30 November, and (d) 1 December 2014. The black star shows the location of Xianghe.

643
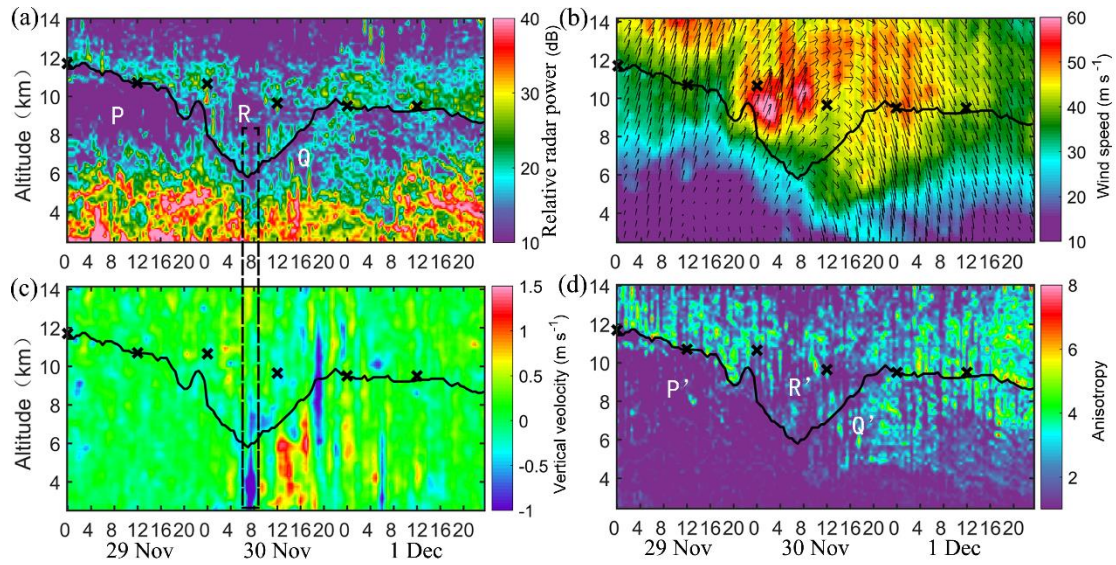
Figure 5. Altitude-time section of (a) the radar backscattered echo power in zenith direction, (b) the horizontal wind speed along with wind vector, of which the up and down arrows represent north and south respectively, and left-right is west-east, (c) the vertical velocity, and (d) the aspect sensitivity, observed by the Beijing MST radar from 29 November to 1 December 2014. The black curve shows the radar-determined tropopause, as defined in section 2.1. The dotted rectangle highlights the strong downdrafts immediately preceding the rapid tropopause ascent. The positions of the LRT tropopause heights, derived from the nearly simultaneous collocated GPS radiosonde temperature profile, are marked by crosses.
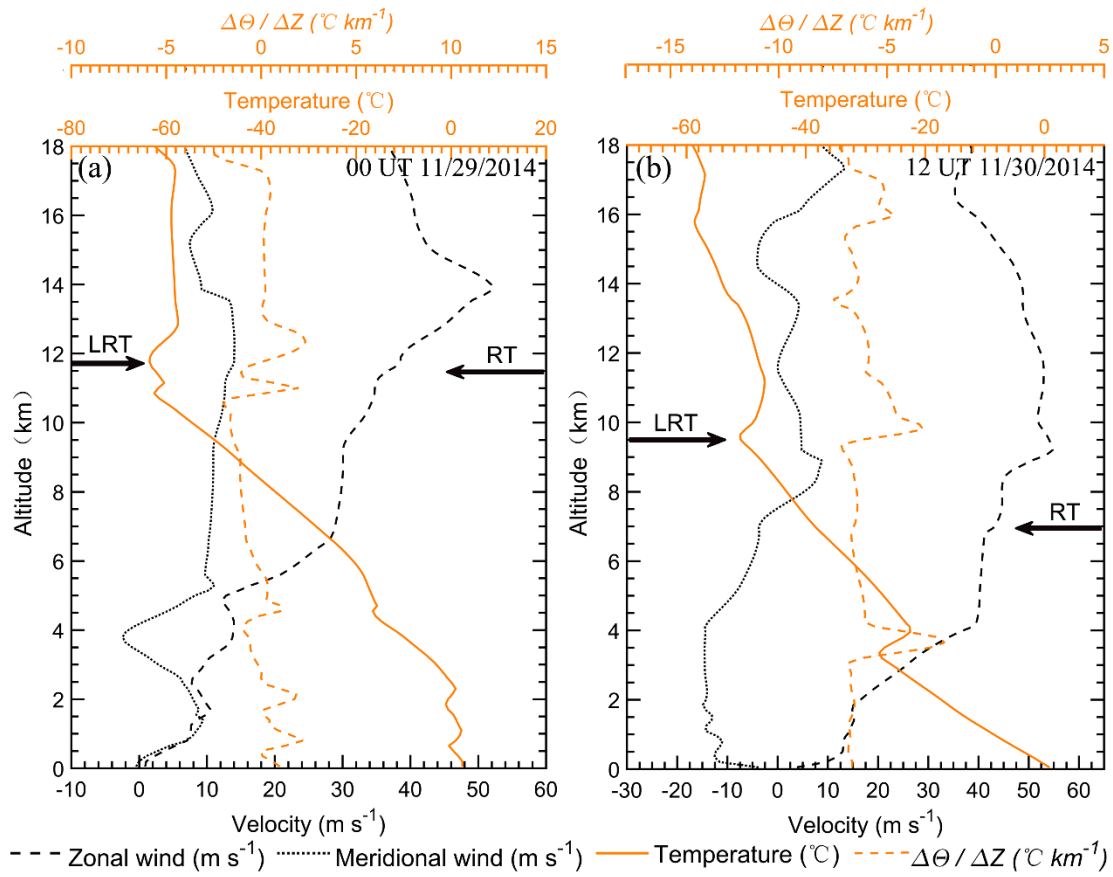
Figure 6. Vertical profiles of zonal wind, meridional wind, temperature, and potential temperature gradient derived from the GPS radiosonde measurements, at (a) 0000 UTC 29 November 2014 and (b) 1200 UTC 30 November 2014. The bold arrows on the left and right side of each panel indicate the radiosonde derived LRT tropopause and radar-derived tropopause height, respectively.
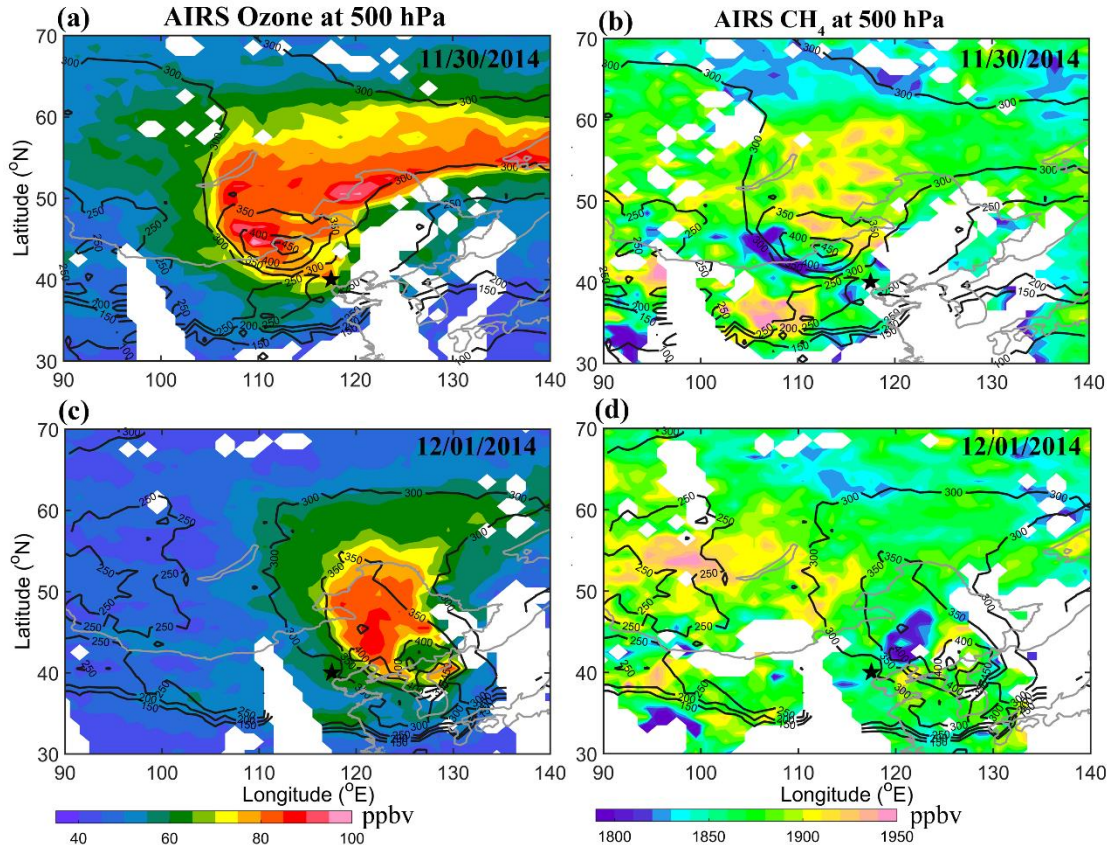
Figure 7. 500 hPa Ozone (left panels) and methane CH$_4$ (right panels) distribution along with the tropopause height contour, derived from the AIRS satellite observations. The top and bottom plots show the data of 30 November 2014 and 1 December 2014, respectively. According to the Aqua Orbit Tracks (not shown), the time range of the satellite passage is between ~04:00-07:25 on 30 November and between ~03:15-06:35 on 1 December 2014. The black star indicates the location of Xianghe.

668
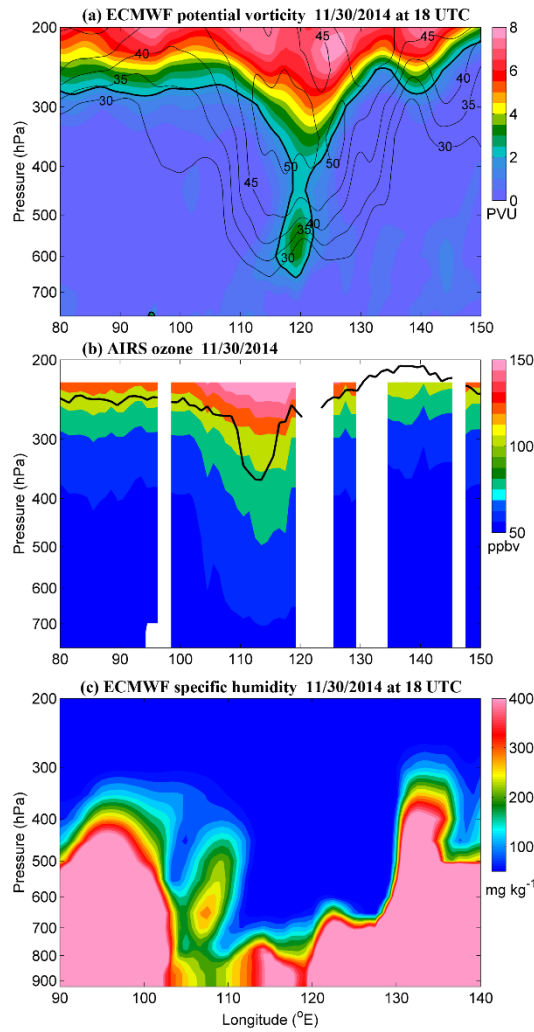
Figure 8. Longitude-pressure cross section of (a) ECMWF PV (colors, in pvu) along

with horizontal wind contour (thin black line, m/s) at 18 UTC on 30 November 2014,

(b) AIRS ozone mixing ratio (colors, in ppbv) along with tropopause height (black line)

on 30 November 2014, and (c) ECMWF specific humidity (colors, in mg kg^{-1}) at 18

UTC on 30 November 2014, at a constant latitude 40° N (nearest grid point in the

latitude of Xianghe). The bold line in (a) marks the isotropic line of PV at 2 pvu.
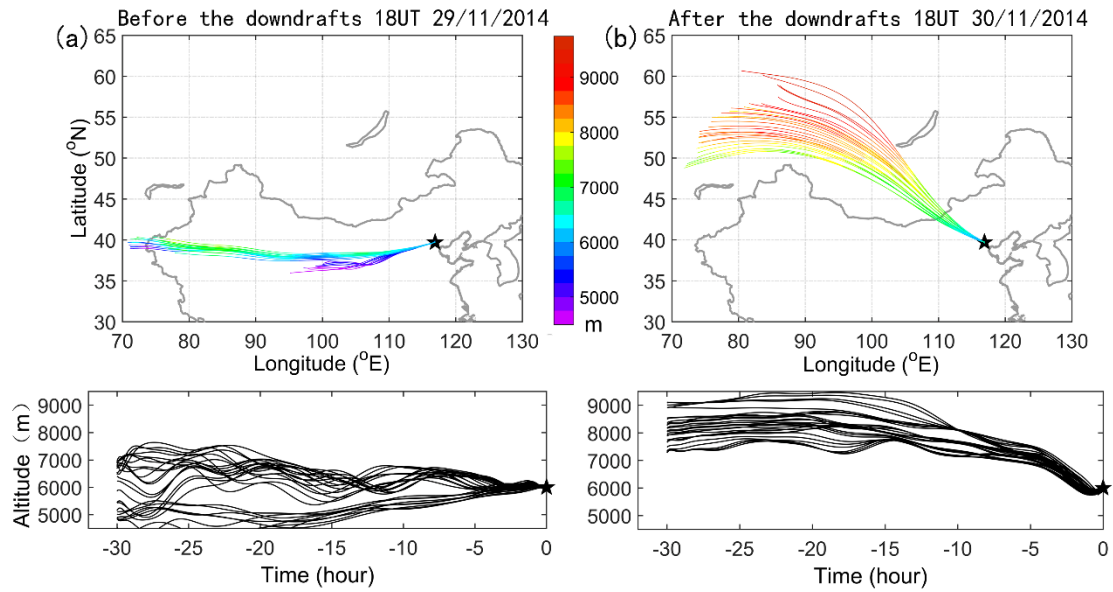
Figure 9. Illustration of 30 h three-dimensional backward trajectories ending at Xianghe at 6000 m using National Oceanic Atmospheric Administration (NOAA) HYSPLIT model: (a) before the main downdrafts at 18 UTC on 29 November 2014, and (b) after the main downdrafts at 18 UTC on 30 November 2014. The HYSPLIT ensemble consists of 27 trajectories. Upper plots show the horizontal projection of the trajectories, and the lower plots show the corresponding time-height vertical displacement of the trajectories.
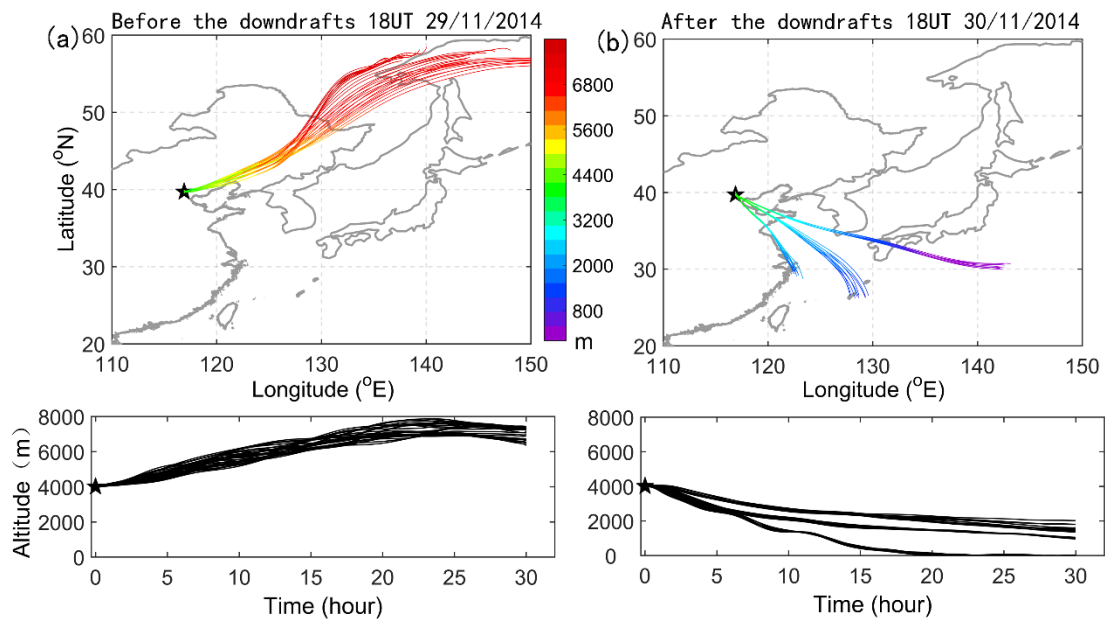
684

685 **Figure 10.** Same as Fig.10 but for three-dimensional forward trajectories starting at

686 Xianghe at 4000 m: (a) before the main downdrafts at 00 UTC on 30 November 2014,

687 and (b) after the main downdrafts at 00 UTC on 1 December 2014.

688
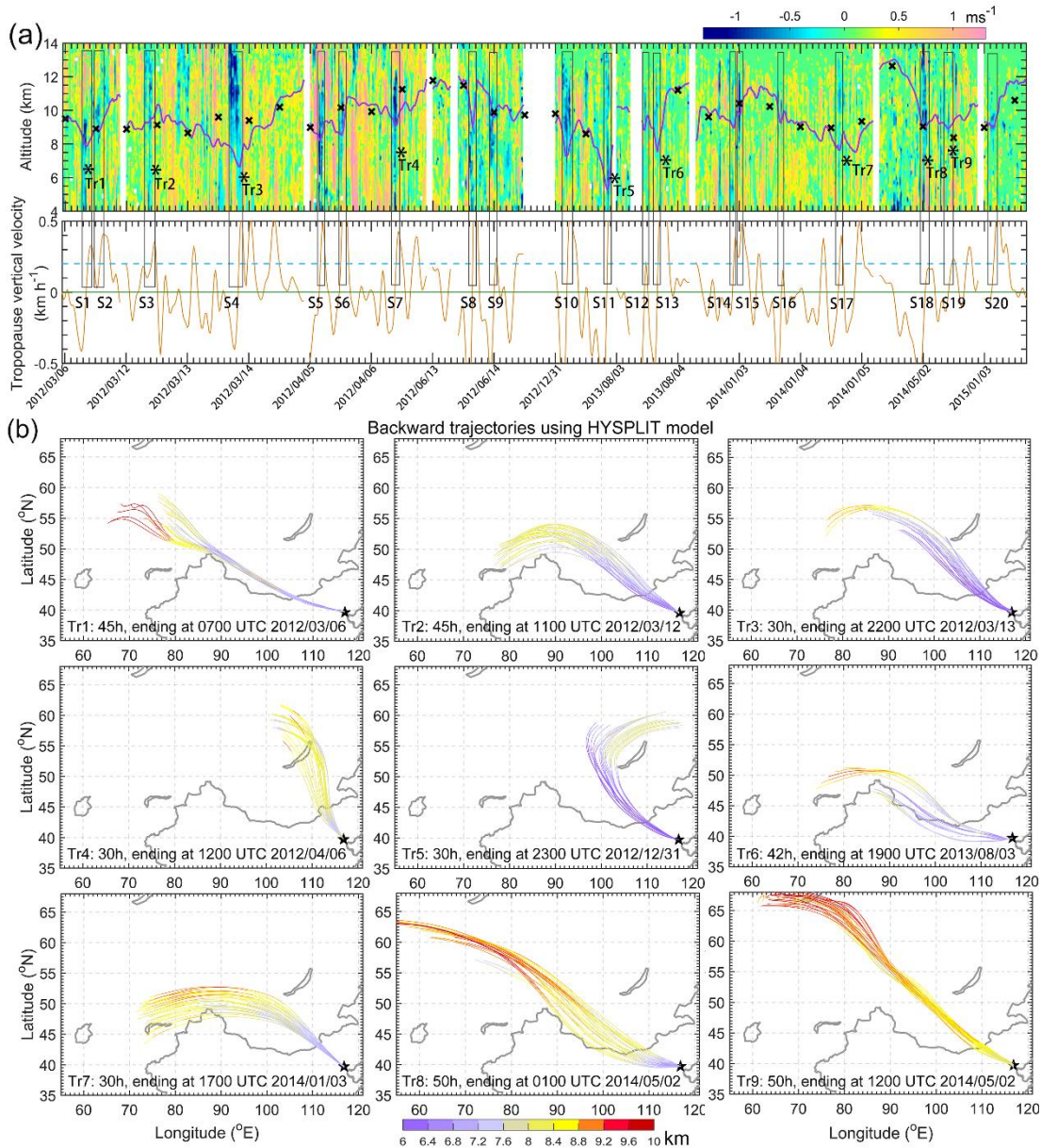
Figure 11. (a) Height-time section of several episodic observations of the radar-derived

vertical wind (colors in m/s) along with RT height (purple bold line) and LRT height

(bold crosses), between March 2012 and Jan. 2015. The corresponding vertical velocity

of the RT (orange line) is plotted in the lower panel of (a), dotted blue line indicates the

value of 0.2 km/h. Dates for the observations are displayed as year/month/day. Black

rectangular boxes represent the cases of strong downdraughts (absolute value ≥ 0.5 m/s)

preceding rapid tropopause ascent (>0.1 km h^{-1}) and are labeled as S1, S2, S3…, S20.

696   Symbol '*' labeled as Tr1-Tr9 indicates the ending point of the corresponding

697   trajectories in Fig.12b. (b) Results of backward trajectories (colors in km) of the typical

698   9 selecting cases from Fig.12a, providing the signature and source of possible

699   stratospheric intrusions.

700

701
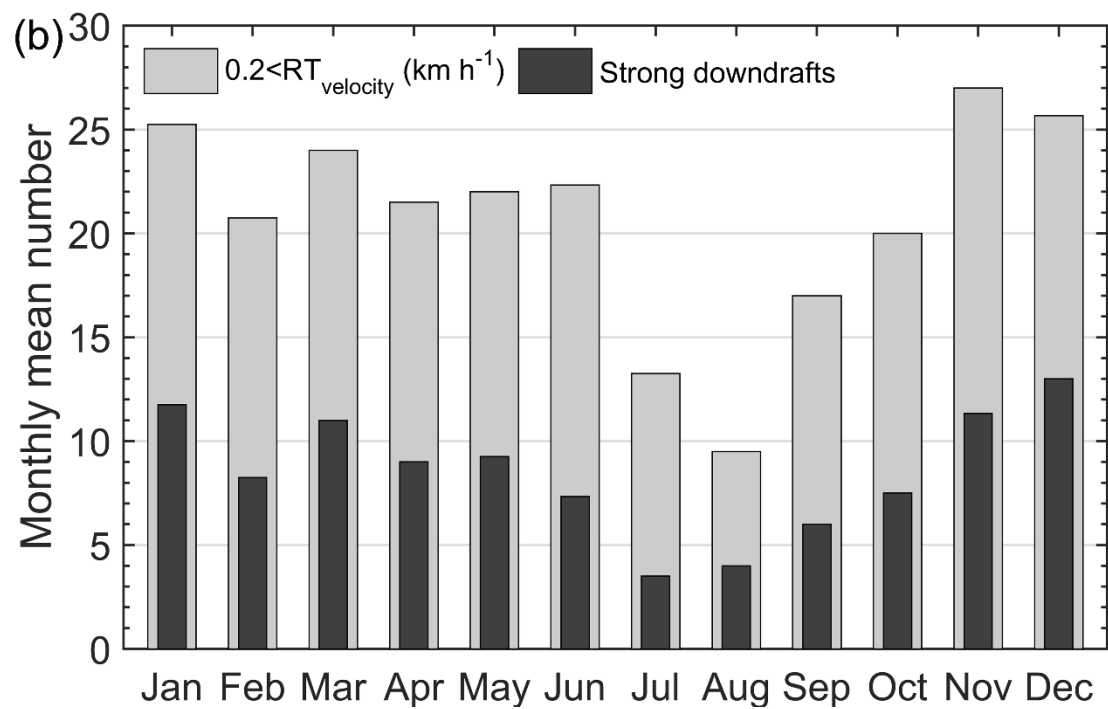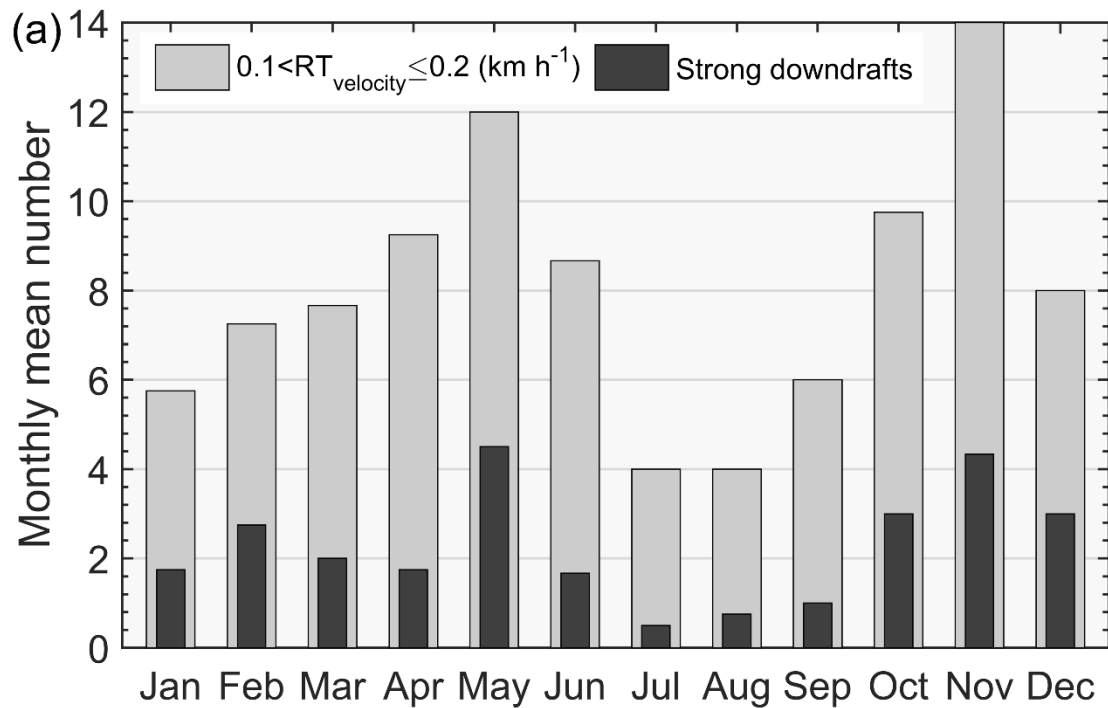
Figure 12. Four years (2012-2015) of radar-determined monthly mean number of rapid

tropopause ascent (gray bands) and the corresponding strong downdrafts just preceding

the rapid tropopause ascent (black bands). (a) Gray bands: with the ascent by at least

0.6 km and the excursion velocity is between 0.1-0.2 km h^{-1}; black bands: except for

the criteria of gray bands, strong downdrafts occurred preceding the rapid RT ascent

707   must exceed 0.5 m s^{-1} and pass through the RT layer. (b) Same as (a) but for the

708   occasions when the ascent velocity is larger than 0.2 km h^{-1}. According to the study

709   here, the black bands in the histogram well represent the occurrence of possible

710   stratospheric intrusions.